Optimized Geometric Structure of a Rotational Hydrodynamic Cavitation Reactor

Y. Wang[1,2], M. Li[1†], H. L. Liu[1], J. Chen[1], L. L. Lv[1], X. L. Wang[1] and G. X. Zhang[1]

[1] *Research Center of Fluid Machinery Engineering and Technology, Jiangsu University, Zhenjiang 212013, China*
[2] *Department of Precision Manufacturing Engineering, Suzhou Vocational Institute of Industrial Technology, Suzhou 215104, China*

†*Corresponding Author Email: 2212011017@stmail.ujs.edu.cn*

ABSTRACT

The objective of this paper is to obtain an excellent structure of a rotational hydrodynamic cavitation reactor (RHCR) by a numerical method and then to investigate the cavitating flow characteristics of the optimized RHCR experimentally. The RNG k-ε turbulence model combined with the Zwart cavitation model was applied to analyze the influence of the straight blade number, the baffle position and the baffle shape on the pressure field, bubble distribution and turbulence kinetic energy of the RHCR. The results show that compared to the original model, an RHCR with a straight blade number of 6, a baffle position of 0.74 and a triangular baffle offers better cavitation performance. Moreover, the energy performance and the cavitation development process of the optimized RHCR were studied experimentally. The results indicate that the multiscale bubbles are induced by straight blades and baffles of the optimized RHCR, accompanied by the twice quasi-periodic shedding dynamics in one cycle. The findings of this study have positive significance for the design and optimization of RHCRs.

Keywords: Rotational hydrodynamic cavitation reactor; Numerical simulation; Experiment; Geometric structure; Cavitation performance.

NOMENCLATURE

F_{cond}	empirical condensation coefficient	α_v	vapor volume fraction
F_{vap}	empirical evaporation coefficient	ρ_l	liquid density
R_B	initial diameter of cavitation bubble	ρ_v	vapor density
R_c	condensation rate	ρ_m	mixture density
R_e	evaporation rate	μ_m	viscosity coefficient of the mixture
α_l	liquid volume fraction	φ	baffle position

1. INTRODUCTION

Cavitation is a unique physical property of liquid due to local pressure drops to saturated vapor pressure, which includes inception, growth, contraction and ultimate collapse (Reiner 1949). Being such a difficult problem, many scholars have studied the unsteady characteristics of cavitation bubbles carefully to reveal their evolution characteristics and laws. Long *et al*. (2018) provided a three-dimensional Lagrangian technology to simulate cavitating flow around a Delft twisted hydrofoil; they revealed the development process of U-type structures and discussed the close relationship between cavitation and vortices. Long *et al*. (2019) studied the unsteady turbulent cavitating flow around a Clark-Y hydrofoil with emphasis on large eddy simulation verification and validation (V&V) analyses and found that the simulation result was in good agreement with the experimental data. Cheng *et al*. (2021) provided a new cavitation model without taking into account the noncondensable gas and modeled the cavitating flow around an elliptical NACA-16020 hydrofoil. They noted that the new cavitation model can better predict tip vortex cavitation. Wang *et al*. (2021a) investigated turbulent cavitating flow around a Clark-Y hydrofoil to study bubble dynamics by using a multiscale Eulerian–Lagrangian method, and their findings revealed detailed information about the effect of turbulent cavitating flow on bubble behavior. All of their contributions have promoted further

understanding of cavitation. Although cavitation can cause many negative effects, including vibration and noise, damaging flow passage components, blocking flow channels, and reducing the efficiency of hydraulic machinery (Guan 2011; Wang *et al.* 2022), it shows enormous potential in sewage treatment (Gagol *et al.* 2018; Kosel *et al.* 2020), medical treatment (Li *et al.* 2021), new energy (Ghorbani *et al.* 2017; Gevari *et al.* 2019), water disinfection (Sun *et al.* 2018) and cell disruption (Mevada *et al.* 2019) on account of the considerable energy released when bubbles collapse. To make better use of cavitation, various cavitation reactors have been invented and applied in these fields. As a superior cavitation reactor, the hydrodynamic cavitation reactor has been used in various fields because of its greenness, affordability, and lower energy consumption. Hydrodynamic cavitation reactors mainly involve orifices (Bhukya *et al.* 2021; Charikleia *et al.* 2021), venturis (Sun *et al.* 2020a; Taba *et al.* 2020), vortex cavitation reactors (Ranade *et al.* 2020; Patil *et al.* 2021) and rotational hydrodynamic cavitation reactors (RHCRs) (Badve *et al.* 2013, Petkovšek *et al.* 2013; Zupanc *et al.* 2014). Orifices and venturis are difficult to widely use because of large pressure loss, clogging, and lower scalability. Similarly, vortex cavitation reactors are less flexible in controlling cavitation and are more likely to be choked; they are also difficult to widely utilize (Agarkoti *et al.* 2021; Wang *et al.* 2021b). An RHCR is capable of generating intense cavitation periodically accompanied by a lower pressure drop and energy dispersion, and it shows obvious advantages over other cavitation reactors.

In recent years, researchers have carried out a large number of experimental and numerical studies on hydrodynamic cavitation reactors. The influence of geometric parameters and operating conditions on cavitation performance has been investigated through visualization experiments and organic degradation experiments. Petkovšek *et al.* (2013) investigated the effect of the angle between two teeth on the cavitation performance of cavitation reactors. They noted that two kinds of cavitation were generated by right-angled teeth and three kinds of cavitation were induced by teeth with an inclination of 8°. In addition, they used a cavitation reactor modified by a centrifugal pump for the pretreatment of waste-activated sludge (Petkovšek *et al.* 2015). The results indicated that the soluble chemical oxygen demand (SCOD) increased substantially when using this cavitation reactor. Gostiša *et al.* (2021a) studied the influence of the pin number, pin diameter, pin surface roughness and rotational speed on the hydrodynamic cavitation performance of a pinned disc RHCR. The results indicated that rotational speed and pin number are the most significant design parameters; however, pin diameter and surface roughness are less significant. Subsequently, they evaluated the cavitation performance of a pinned disc RHCR in comparison with a serrated disc RHCR on a pilot scale (Gostiša *et al.* 2021b). They observed that supercavitation occurred surrounding the cylinders of the pinned disc rotor, and the pinned disc can generate more intense cavitation than a serrated disc while consuming less

energy per liquid pass. Kim *et al.* (2020) revealed the cavitation–generation mechanism of a rotor–stator hydrodynamic cavitation reactor by using a flow visualization experiment, and they studied the effects of cavitation and shear stress on sludge disintegration for reactors with and without dimples. The results suggested that the SCOD of the sludge dramatically increased with the use of dimples. Sun *et al.* (2020b) investigated the effects of rotational speed and flow rate on the thermal performance of an advanced rotational hydrodynamic cavitation reactor (ARHCR) and evaluated the disinfection performance of *Escherichia coli*. The results showed that a critical flow rate exists for the present ARHCR, and the present ARHCR offers high treatment efficiency.

For numerical investigations into cavitation reactors, many interesting works have been conducted to understand the complex cavitation generation mechanism and reveal the effects on cavitation performance. Simpson and Ranade (2018) investigated the effects of orifice thickness, hole inlet sharpness and wall angle on cavitation behavior. They noted that orifice thickness has a significant influence on cavitation behavior, and inlet radius similarly has an obvious effect on cavitation performance. Dutta *et al.* (2021) proposed and studied three different strategies to enhance cavitation intensity in a circular venturi. They observed that the surface roughness on the trumpet diverging wall obviously influences the cavitation intensity in comparison with other designs. Badve *et al.* (2015) used the Navier–Stokes method to investigate the flow characteristics of a stator and rotor hydrodynamic cavitation reactor. The results suggest that the characteristics of the shear rate and pressure field are quite different at different rotational speeds of the rotor. Sun *et al.* (2021a) elaborated the cavitation generation mechanism and interaction process of an ARHCR. They noted that the sheet cavitation generated on the downstream sides of both the moving and static cavitation generation units (CGU) and vortex cavitation formed in the vortex center of each CGU are the main cavitation forms of this ARHCR. Then, they investigated the shapes, diameters, interaction distances, heights, and inclination angles of the CGU on cavitation performance (Sun *et al.* 2021b). The best structure with the highest cavitation performance was obtained. Finally, they carried out multiobjective optimization involving diameter D, interaction distance s, height h, and inclination angle θ of the CGU by combining a genetic algorithm and CFD method (Sun *et al.* 2021c). The results indicated that smaller s and greater θ in proper ranges always benefit the cavitation performance. Song *et al.* (2022) investigated the influence of the cavitation generating unit (CGU) shape, interaction distance and rotor speed on the cavitation intensity and the cavitation energy efficiency of a novel rotor radial groove hydrodynamic cavitation reactor by using the realizable k-ε turbulence model and Zwart cavitation model. They observed that the cavitation performance of rectangular-shaped CGUs was better than that of cylindrical-shaped CGUs, and increasing the rotor speed and decreasing the interaction
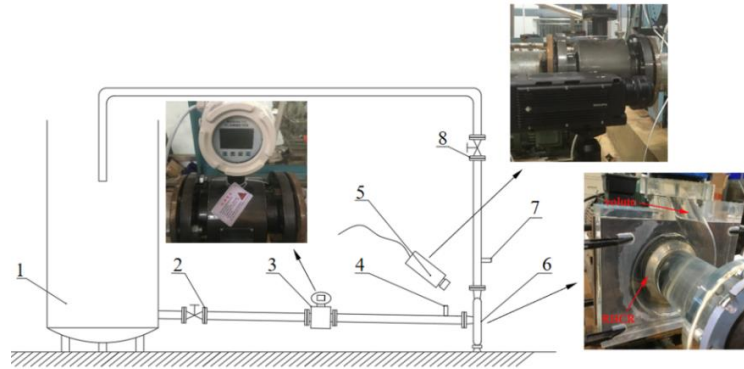
Fig. 1. Schematic diagram of the experimental setup (1- 1500 L tank; 2,8- Valve; 3- Electromagnetic flow meter; 4,7- Pressure transducer; 5- High-speed camera; 6- Centrifugal cavitation pump).

distance can improve the cavitation performance more effectively.

Although researchers have conducted many interesting studies on RHCRs, there is little research on RHCRs evaluating both energy performance and cavitation performance. Most studies have solely focused on the cavitation performance of RHCRs and ignored energy performance. As a result, it is necessary to use other equipment to continuously transport fluid. In addition, some RHCRs can only achieve low cavitation intensity at a higher speed, which is difficult to apply in practice.

Inspired by a previous study, a novel RHCR that easily induces intense cavitation by baffles and has good energy performance is designed. The objective of this paper is to obtain an excellent RHCR structure by a numerical method and then to investigate the cavitating flow characteristics of the optimized RHCR by an experimental method. The geometric parameters of the RHCR involve the straight blade number, and the baffle position and the baffle shape affecting the cavitating flow are analyzed. Finally, the energy performance and details of the cavitation development process of the optimized RHCR are further studied experimentally.

2. EXPERIMENTAL SETUP AND NUMERICAL METHOD

2.1 Experimental Setup

The experiment is carried out on the open test bench at the National Pump and System Engineering Technology Research Center of Jiangsu University. A schematic diagram of the experimental setup is shown in Fig. 1. The centrifugal cavitation pump (CCP) contains a volute, and the optimized RHCR is the core component of the system. To visualize the internal flow field, the CCP is made of transparent silica glass with high transmittance. A water storage tank with a volume of 1500 L is applied for the circulating water. The inlet valve is installed close to the tank to regulate the inlet pressure, which is measured by the MIK-P3000 pressure transducer with a measurement accuracy of 0.075%, and achieve the desired cavitation condition of the CCP. The mass flow rate of the line is regulated by the outlet valve employed on the closed-circuit pipeline

away from the outlet of the CCP, the value of which is measured by a CKLDG-D100-TL electromagnetic flow meter with a measurement accuracy of 0.04%.
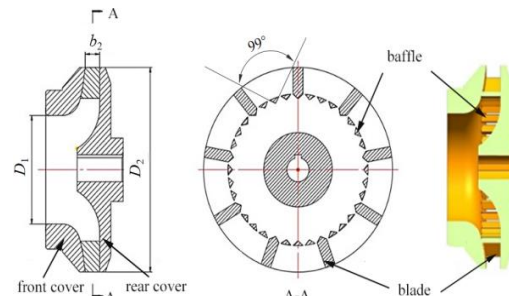

Fig. 2. Structure of the RHCR.

An MIK-3051-CP pressure transducer with a measurement accuracy of 0.075% is installed close to the outlet of the CCP for measuring the outlet pressure, which can be combined with the inlet pressure for calculating the head. The cavitation development process is revealed explicitly by visualization with a MotionProY4 high-speed camera with an image acquisition rate of 350,000 fps, and an image acquisition rate of 4500 fps under the design working condition is utilized for the experiment.

2.2 Rotational Hydrodynamic Cavitation Reactor

The present study modifies the impeller of a centrifugal pump with a specific speed of n_s= 117.3 and obtains a new type of RHCR with a mass flow rate of 60 m³/h, rotational speed of 2300 rpm and head of 4.4 m. This new cavitation reactor with an inlet diameter D_1 of 90 mm, outlet diameter D_2 of 170 mm and outlet width b_2 of 13 mm mainly contains a front cover and a rear cover and is equally equipped with 9 straight blades and 27 triangular baffles curved back along the circumference. Its original structure is shown in Fig. 2. At the inlet of the RHCR, the triangular baffles are evenly arranged parallel to the axis in a circumferential direction, and the structure resembles Venturi's throat (which will be called throat in the following passages), which is formed between the baffle and the baffle, the baffle

and the straight blade. The baffle position φ is 0.71, where φ refers to the ratio of the maximum outer diameter of the baffle to the outlet diameter of the RHCR, and the top angle of the baffle is 99°. To investigate the effect of geometric parameters on the cavitating flow characteristics of this RHCR, the straight blade number (3, 4, 6, 9 and 12), the baffle position φ (0.67, 0.71, 0.74 and 0.78) and the baffle shape (triangle and circle) are analyzed in this paper.

2.3 Numerical Method

2.3.1 Governing Equations

As one of the most representative models in the Euler–Euler approach, the homogeneous model allows all fluids and other relevant fields (such as temperature and turbulence) to share a common flow field, which simplifies the multifluid model and results in a homogeneous model. The continuity and momentum equations of the mixture are as follows:

$$\frac{\partial \rho_m}{\partial t} + \frac{\partial (\rho_m u_j)}{\partial x_j} = 0 \qquad (1)$$

$$\frac{\partial (\rho_m u_i)}{\partial t} + \frac{\partial (\rho_m u_i u_j)}{\partial x_j} = -\frac{\partial p}{\partial x_i} + \\ \left[(\mu + \mu_t) \left(\frac{\partial u_i}{\partial x_j} + \frac{\partial u_j}{\partial x_i} - \frac{2}{3} \frac{\partial u_i}{\partial x_j} \delta_{ij} \right) \right] \qquad (2)$$

where ρ_m is the mixture density, $\rho_m = \rho_l \alpha_l + \rho_v \alpha_v$, $\alpha_l + \alpha_v = 1$, ρ_l is the liquid density, ρ_v is the vapor density, α_l is the liquid volume fraction, and α_v is the vapor volume fraction. u_i and u_j are the velocity components in the i and j directions under the Cartesian coordinate system. μ_m is the viscosity coefficient of the mixture, and $\mu_m = \mu_l \alpha_l + \mu_v \alpha_v$.

2.3.2 Turbulence and Cavitation Models

The RNG k-ε turbulence model is an improvement based on the standard k-ε turbulence model, which adds an R term to the standard k-ε model to consider the effect of a high turbulence strain rate, resulting in good accuracy in forecasting complex turbulence such as rotating and large curvature flows (Smit *et al.* 1992). The RNG k-ε turbulence model has a great advantage in simulating turbulence due to shear motion in the gap (Sawant *et al.* 2008), and the equations are defined as follows:

$$v_t = C_\mu \frac{k^2}{\varepsilon} \qquad (3)$$

$$\frac{\partial k}{\partial t} + u_j \frac{\partial k}{\partial x_j} = \\ \frac{\partial}{\partial x_j} \left[\left(v + \frac{v_t}{\sigma_k} \right) \frac{\partial k}{\partial x_j} \right] + G_k - \varepsilon \qquad (4)$$

$$\frac{\partial \varepsilon}{\partial t} + u_j \frac{\partial \varepsilon}{\partial x_j} = \frac{\partial}{\partial x_j} \left[\left(v + \frac{v_t}{\sigma_\varepsilon} \right) \frac{\partial \varepsilon}{\partial x_j} \right] + \\ C_{\varepsilon 1} \frac{\varepsilon}{k} G_k - C_{\varepsilon 2} - R \qquad (5)$$

$$R = \frac{\eta \left(1 - \frac{\eta}{\eta_0} \right)}{1 + \beta \eta^3} \frac{\varepsilon}{k} G_k \qquad (6)$$

$$\eta = \frac{S_k}{\varepsilon} \qquad (7)$$

$$S = \sqrt{2 \overline{S_{ij} S_{ij}}} \qquad (8)$$

$$\overline{S_{ij}} = \frac{1}{2} \left(\frac{\partial u_i}{\partial x_j} + \frac{\partial u_j}{\partial x_i} \right) \qquad (9)$$

where $C_{\varepsilon 1}$=1.42, $C_{\varepsilon 2}$=1.68, C_μ=0.0845, σ_κ=0.7179, σ_ε=0.7179, η_0=4.38, and β=0.012.

The Zwart cavitation model (Zwart *et al.* 2004) utilizes the density of bubbles to calculate the interphase mass transfer rate per unit volume and ignores the quadratic derivative of the bubble diameter with time in the simplified Rayleigh–Plesset equation, which has the following governing equations:

$$R_e = F_{vap} \frac{3\alpha_{nuc}(1 - a_v)}{R_B}, P_0 \le P_V \qquad (11)$$

$$R_c = F_{cond} \frac{3 a_v \rho_v}{R_B} \left(\frac{2}{3} \frac{P_0 - P_V}{\rho_l} \right), P_0 > P_V \qquad (12)$$

where the same parameters refer to the same meaning as the above description. R_e and R_c are the evaporation rate and condensation rate, respectively. F_{vap} and F_{cond} are the empirical evaporation coefficient and empirical condensation coefficient with values of 50 and 0.01, respectively, α_{nuc} is the volume fraction of the noncondensable gas nucleus, and R_B is the initial diameter of the cavitation bubble with a value of 1×10^{-6} m.

2.3.3 Computational Domain and Boundary Conditions

To promote the convergence of the calculation and improve the accuracy of the results, extension sections as stationary domains are employed on the inlet of the RHCR and outlet of the volute, and the lengths of the suction pipe and discharge pipe are at least 5 times their diameters. All computational domains are shown in Fig. 3. The commercial software ANSYS CFX18.2 is applied to predict the internal cavitating flow of the CCP. A pressure inlet with a total pressure of 0.0875 MPa is adopted for the inlet boundary, and a mass flow rate of 60 m³/h is utilized for the outlet boundary. The RHCR is specified as the moving domain rotating on the axis
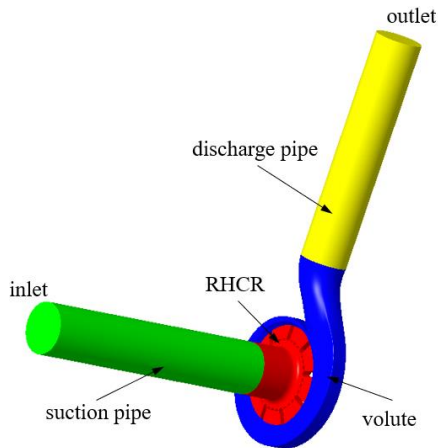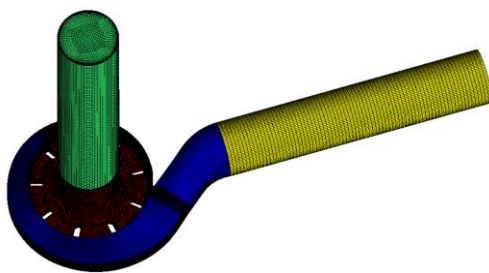
Fig. 3. Computational domains of the CCP.

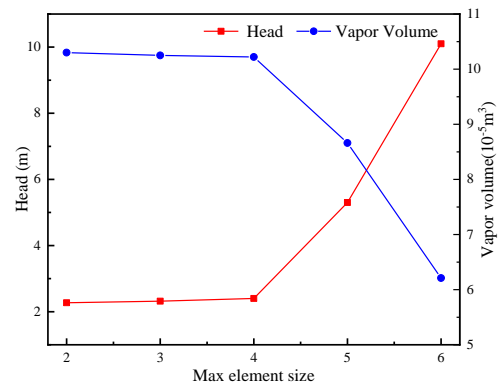Fig. 4. Grids of computational domains.

Fig. 5. Change of the head and vapor volume in maximum element size.

Table 1 The head difference between cavitation calculation result and experimental result of the centrifugal pump

Mass flow rate(kg/m³)	Numerical result(m)	Experimental result(m)	η (%)
65	8.1	8.5	4.7
60	12.3	12.9	4.6
55	15.8	16.5	4.2

with a constant rotational speed of 2300 rpm. Dynamic and static coupling between the inlet extension section and RHCR, RHCR and volute is achieved by setting up the frost rotor interface. All other faces are set to walls with no-slip conditions, and the wall roughness is assumed to smooth the wall. The scalable wall function is used for the near-walled area. The result of the steady calculation of the no-cavitation model is used as the initial value of the cavitation calculation, and the inlet boundary is appended with a liquid phase volume fraction of 1 and a vapor volume fraction of 0. A saturated vapor pressure of 3169 Pa is set as the critical condition for cavitation.

2.3.4 Grid-Independence Test

The grids of the computational domains are shown in Fig. 4, unstructured mesh is used to generate the grids of impeller, and structured mesh is used for generating grids of other fluid domains.The RHCR provided in this paper takes into account both the energy performance and cavitation performance, so the head reflecting the energy performance and the vapor volume reflecting the cavitation performance are selected for the grid-independence test. Because the geometric models are not consistent in each case, the maximum element size is chosen to distinguish the differences in meshes instead of the total number of meshes. Figure 5 demonstrates the effect of the maximum element size on the head and vapor volume of the original structure, which clearly shows that the head keeps decreasing with the decrease in

the maximum element size, and the head tends to be steady as the maximum element size is smaller than 4, on the contrary, the vapor volume keeps increasing with the decrease in the maximum element size, and tends to be steady as the maximum element size is smaller than 4. Therefore, considering the calculation efficiency and accuracy, we choose a grid with a maximum element size of 4 for subsequent calculations.

3. RESULTS AND DISCUSSION

3.1 Verification of Numerical Method

The RHCR provided in this paper is designed based on the structure of centrifugal pump by using numerical method, the structure difference between the RHCR and centrifugal pump is not large, unlike the centrifugal pump, more attention has been paid to the cavitation generation mode and cavitation intensity of the RHCR, which can be seen from the characteristics of the internal flow field, so the same numerical method is used to predict the flow field of the RHCR. Because the cavitation experiment of the centrifugal pump is conducted in the previous work, the cavitation calculation result of centrifugal pump using the same numerical method as the RHCR is compared with the experimental result to verify the numerical method, Table 1 shows the head difference between cavitation calculation result and test result of the centrifugal pump, the rotational speed of centrifugal pump is 2300 rpm, the head decreases faster with the increase of mass flow rate, the possible reason is that cavitation is more serious under large mass flow rate, but the head difference between the numerical calculation and experiment is kept within 5%, showing that the numerical method is reliable.
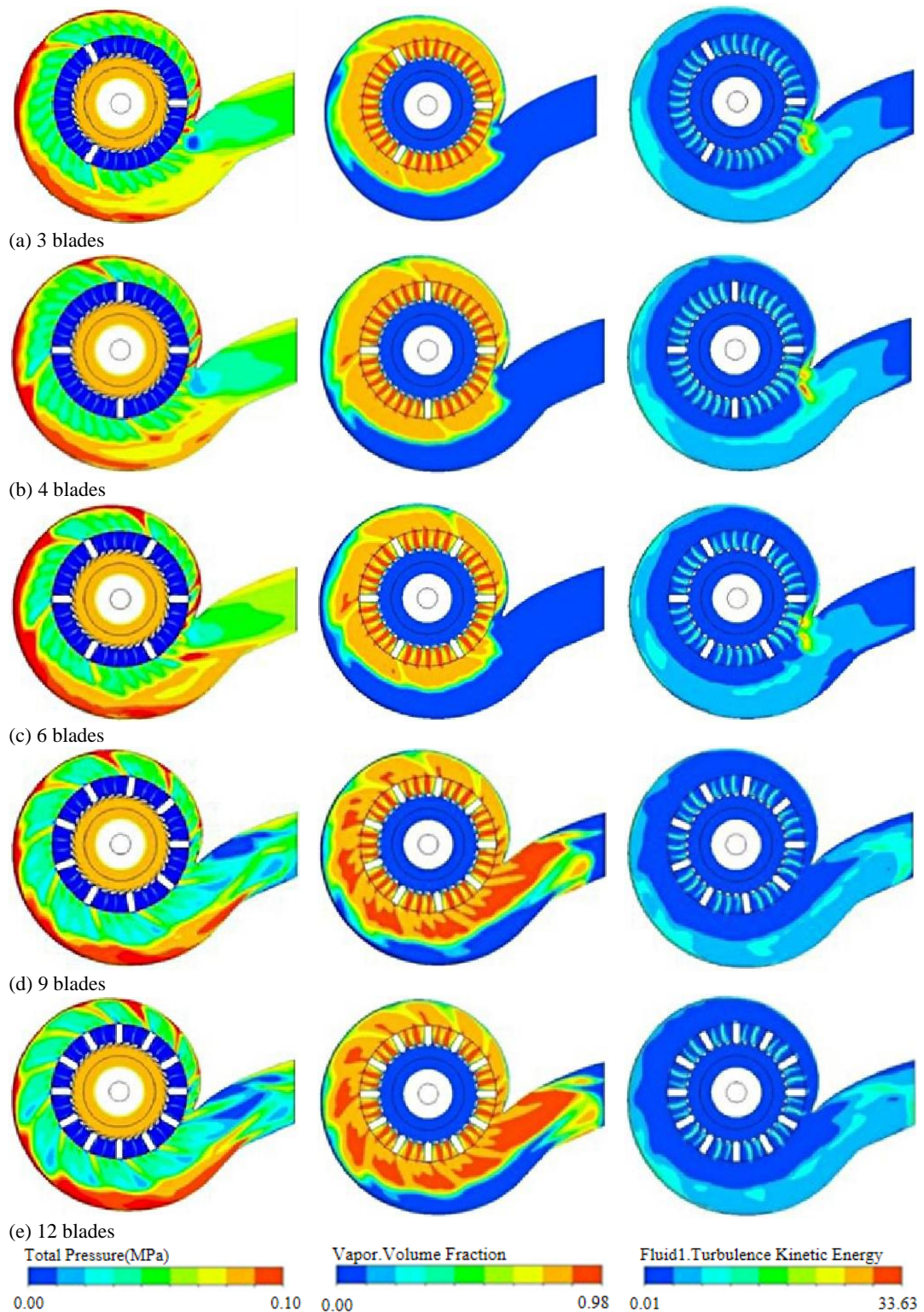
(a) 3 blades

(b) 4 blades

(c) 6 blades

(d) 9 blades

(e) 12 blades

Total Pressure(MPa)

0.00   0.10

Vapor.Volume Fraction

0.00   0.98

Fluid1.Turbulence Kinetic Energy

0.01   33.63

Fig. 6. Effect of the straight blade number on cavitating flow of CCP (left- pressure field; middle-bubbles distribution; right- turbulence kinetic energy).

3.2 The Factors of RHCR Affecting the Cavitating Flow of CCP

3.2.1 The Straight Blade Number

When the fluid attacks the baffle at a certain angle, flow separation occurs at the side of the baffle, resulting in shear cavitation. Then, the fluid passes through the throat, the speed increases sharply, and the pressure drops rapidly, resulting in shrinkage cavitation. The combination of the two effects gives the RHCR a strong cavitation capacity.

Figure 6 illustrates the effect of the straight blade number on the pressure field, bubble distribution and
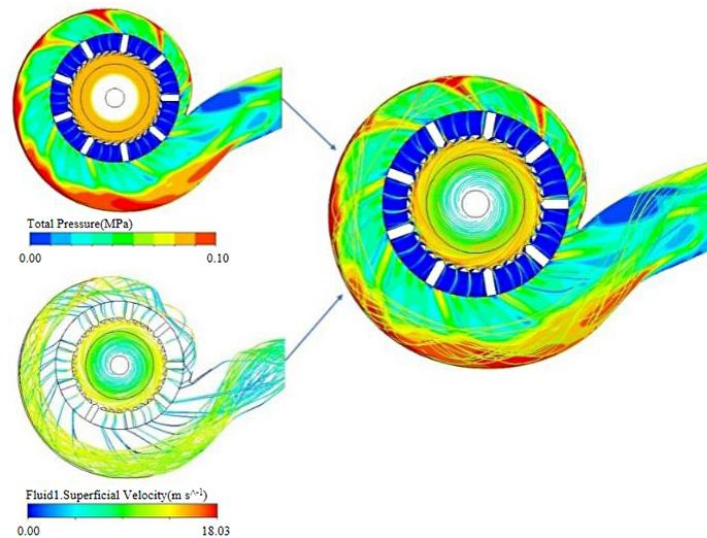
Fig. 7. Pressure field combined with the streamline of CCP with 9 straight blades.

turbulence kinetic energy of the CCP at the same time. The pressure field of the CCP in all cases can be divided into 4 zones, namely, upstream of the baffle, downstream of the baffle, inner edge of the volute and outer edge of the volute. The pressure decreases first as liquid passes through the throat because of the throttling effect, and then kinetic energy and pressure energy increase due to working by the straight blades; thus, the pressure gradually rises at the inner edge of the volute. Finally, the pressure at the outer edge of the volute continues to rise on account of the constraint of the volute, as shown in Fig. 6, left. Several high-pressure areas exist in the volute for each case, and most of them emerge at the end of the straight blade, terminate at the outer edge of the volute accompanying evolution and expand along the direction of rotation, which strongly confirms that the high pressure in the volute and even the outlet pressure of the volute are indeed provided by the straight blades.

Increasing the straight blade number initially increases the high-pressure area at the outer edge of the volute but subsequently decreases, and the largest high-pressure area occurs with 6 straight blades, which can be attributed to the following reasons. Although the increasing number of straight blades provides the liquid more pressure energy, too many blades also narrow the flow channel. Irregular vortexes are more likely to be induced under the effect of the wall surface; as the pressure in the vortex drops lower than saturated vapor pressure, cavitation generates and results in bubbles blocks in the RHCR. Therefore, when the straight blade number does not exceed 6, the blades play a dominant role in liquid pressurization. The pressure on the outer edge of the volute increases slowly with the increasing blades, as shown in Fig. 6(a) to (c), left, when the straight blade number exceeds 6; cavitation enhances sharply, which completely counteracts the effect of the increasing blades on the pressure rise. Eventually, the pressure at the outer edge of the volute does not rise but falls, as shown in Fig. 6(d) to (e), left. This discrepancy is further analyzed in conjunction with the pressure contour

and the streamline of 9 straight blades, as shown in Fig. 7. The streamlines from the throat to the middle of the volute are sparsely radial, indicating that the liquid velocity here is low, which is attributed to the accumulation of bubbles downstream of the baffle. The radial streamlines extend all the way to the volute outlet, indicating that the high-speed liquid mixed with bubbles has expanded to the volute outlet, reducing the outlet pressure of the RHCR, which is not conducive to bubble collapse and energy release, leading to poor energy performance.

The bubble distribution does not change significantly with increasing blades as the blade number does not exceed 6, and the high vapor volume faction bubbles accumulate downstream of the baffle, as shown in Fig. 6(a) to (c), middle. However, the cavitation area apparently expands when the blade number exceeds 6, and the high vapor volume fraction bubbles gradually diffuse into the volute and ultimately extend to the volute outlet, as shown in Fig. 6(d) to (e), middle. The bubble distributions of 6 and 9 straight blades with vapor volume fractions greater than 0.5 are isolated separately to further discuss the effect of the number of straight blades on cavitation, as shown Fig. 8. For the 6 blades, the high vapor volume fraction bubbles are evenly distributed downstream of the baffle, followed by the inner edge of the volute and other areas, and all the bubbles gather steadily and evenly in the spiral area of the volute. For the 9 straight blades, the high vapor volume fraction bubbles in the volute are distributed in a strip (which will be called the strip cavitation area in the following passages), and some of the strip cavitation areas even connect with the strips in the RHCR. After numbering the strip cavitation areas in the volute, it is found that the number is equivalent to the total number of entities from the corresponding straight blade clockwise to the corresponding baffle, which confirms that the strip cavitation areas in the volute are indeed induced by straight blades and baffles. Cavitation will intensify sharply as the blade number exceeds 6, reducing the overall pressure of the volute and affecting the liquid delivery.
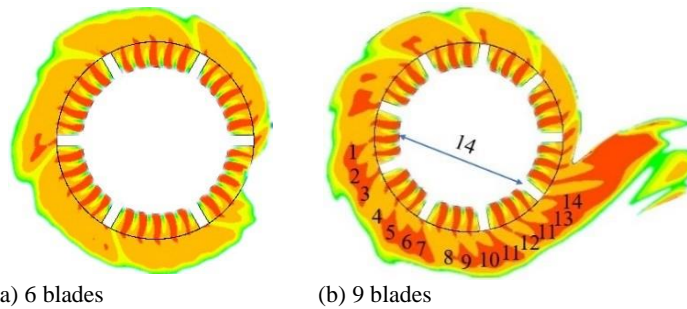
(a) 6 blades   (b) 9 blades

Fig. 8. Bubble distribution of the CCP with 6 and 9 straight blades with vapor volume fractions. greater than 0.5.

Turbulence kinetic energy can also reflect cavitation intensity. As cavitation occurs, the flow field of the cavitation area is extremely disordered due to the vapor–liquid two-phase interaction; additionally, the nonlinear motion and collapse of bubbles will also endow the flow field with strong disturbance, which causes large turbulent kinetic energy. As depicted in Fig. 6, right, one larger turbulence kinetic energy exists in the back of the baffle, which can be attributed to the vortex cavitation induced by the baffle, and another larger turbulence kinetic energy exists at the outer edge of the volute due to bubble collapse, as shown in Fig. 6, middle. For 3, 4 and 6 blades, the largest turbulence kinetic energy appears near the tongue because the linear motion of the liquid followed by the bubbles with less nonlinear vibration is dominant at the inner edge of the volute. However, on account of the smaller circulation area near the tongue, the dynamic and static interference between the RHCR and the volute is intensified significantly, leading to greater turbulence kinetic energy, as shown in Fig. 6(a) to (c), right. For 9 and 12 blades, the turbulence kinetic energy at the volute outlet increases obviously but decreases near the tongue, as depicted in Fig. 6(d) to (e), right, because for these cases, the vapor–liquid mixture continues to accumulate at the outer edge of the volute with little velocity, and the bubbles contract and collapse at the volute outlet.

In summary, the straight blade number has an important effect on the energy and cavitation performance of the CCP, and increasing the straight blade number will increase the cavitation intensity. However, too many straight blades cause bubble accumulation at the volute outlet, which is not conducive to the transport of liquid, so an RHCR with 6 straight blades is optimal.

3.2.2 The Baffle Position

The baffle position directly affects the length of the straight blade, which affects the energy conversion reversely and ultimately influences the energy and cavitation performance. According to the analysis of Section 3.2.1, the differences between the energy and cavitation performance of the CCP with baffle positions φ of 0.67, 0.71, 0.74 and 0.78 are investigated at the same time by selecting the RHCR with 6 straight blades. When studying the effect of the baffle position on the cavitation flow, the baffle

shape, size and throat shrinkage remain unchanged, and only the distance from the back of the baffle to the center of the impeller changes.

With the increase in φ, the pressure field of the CCP initially does not change significantly, as Fig. 9(a) to (b), left illustrates, and then the pressure in the volute gradually decreases, as shown in Fig. 9(c) to (d), left, which can be attributed to the following reason. For a smaller φ, the straight blades play a dominant role in the flow field, but the throat affects the flow field gradually with a larger φ. This is because the throat is further away from the inlet of the RHCR as φ is larger, leading to larger liquid velocity before the throat, which can be obviously observed from streamlines in Fig. 10, and a more intense throttling effect is induced after passing through the throat. Therefore, the pressure downstream of the baffle is further reduced and eventually affects the pressure field in the volute. The streamlines of φ =0.71, 0.74 and 0.78 are chosen for further analysis in consideration of great differences in the pressure field among these three cases. For φ =0.71, the streamlines downstream of the baffle are extremely disordered, and the spiral streamlines in the volute are evenly distributed along the flow channel with small velocity because bubbles have collapsed inside the RHCR before the mixture enters the volute, and all kinetic energy has been converted into pressure energy, as shown in Fig. 9(b). This case shows strong energy performance but poor cavitation intensity. For φ =0.74 and 0.78, the streamlines downstream of the baffle to the inner edge of the volute are uniformly radial with small velocity, indicating that a large number of bubbles accumulate in this region and remain relatively steady, which can be seen in Fig. 9(c) to (d); therefore, lower pressure is maintained at the inner edge of the volute. In addition, the radial streamlines of φ =0.78 extend downstream of the tongue, demonstrating that bubbles have spread here, resulting in lower pressure at the outlet of the volute and incapability in effectively conveying liquid.

Figure 9, middle presents the effect of φ on bubble distribution. A small number of bubbles exist only downstream of the baffle with smaller φ, leading to weak cavitation intensity, as shown in Fig. 9(a) to (b), middle, which can be reflected in the turbulence kinetic energy in Fig. 9(a) to (b), right. The high turbulence intensity area gathers near the RHCR, indicating that the bubbles have collapsed near the RHCR. For φ =0.74, the high vapor volume fraction.

(a) φ =0.67

(b) φ =0.71

(c) φ =0.74

(d) φ =0.78

Total Pressure(MPa)

0.00   0.10

Vapor.Volume Fraction

0.00   0.98

Fluid1.Turbulence Kinetic Energy
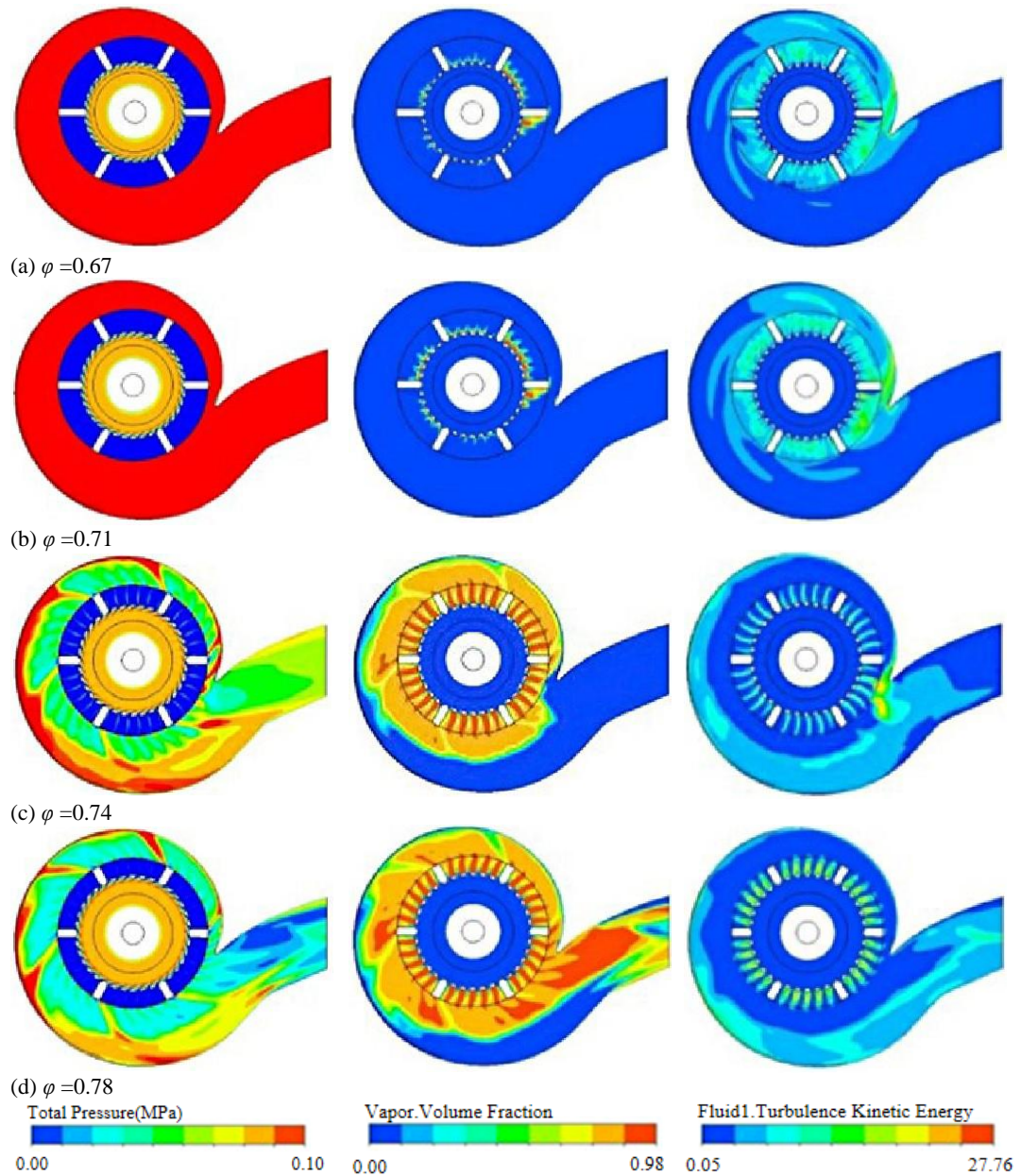
0.05   27.76

Fig. 9. Effect of the baffle position on cavitating flow of CCP (left- pressure field; middle- cavitation distribution; right- turbulence kinetic energy).
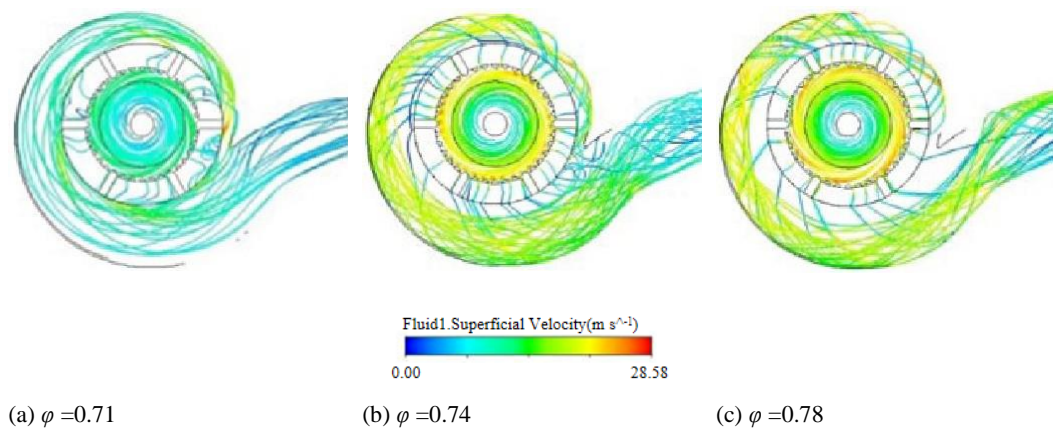
Fluid1.Superficial Velocity(m s^-1)

0.00   28.58

(a) φ =0.71   (b) φ =0.74   (c) φ =0.78

Fig. 10. Streamlines of CCP with baffle positions of 0.71, 0.74, 0.78.
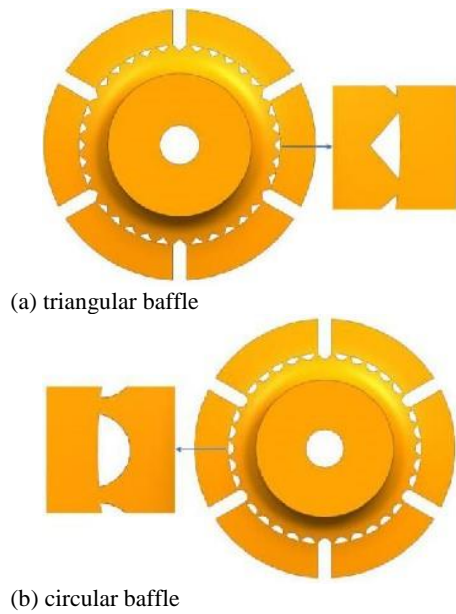
(a) triangular baffle

(b) circular baffle

Fig. 11. Computational domains of RHCRs with triangle baffle and circular baffle.

bubbles filled the entire flow channel downstream of the baffle and even tended to the inner edge of the volute, as shown in Fig. 9(c), middle, both downstream of the baffle and the outer edge of the volute maintain high turbulence kinetic energy, as shown in Fig. 9(c), right. The former can be attributed to the massive vortices induced by the throat, and the latter is because a large amount of bubbles collapse at the outer edge of the volute. When φ is increased to 0.78, the high vapor volume fraction bubbles spread to the inner edge of the volute and even spread to the outlet of the volute, as

shown in Fig. 9(d), middle; simultaneously, the high turbulence kinetic energy region also spreads to the outlet of the volute, indicating the collapse of bubbles in this region. In addition, the turbulent kinetic energy near the tongue in all cases is larger except for φ =0.78, which can be explained through the streamlines in Fig. 10. For φ =0.78, the streamlines near the tongue are sparse because of a large number of bubbles near the tongue, leading to a small mixture velocity. Therefore, the dynamic and static interference is weak near the tongue. In contrast, the streamlines of other cases are disordered due to fewer bubbles close to the tongue, and the liquid flow is dominant, causing intense dynamic and static interference.

In summary, increasing φ significantly increases the cavitation intensity but also weakens the energy performance, and the energy performance and cavitation intensity can be better guaranteed with φ =0.74

3.2.3 The Baffle Shape

According to the analysis of Section 3.2.1 and Section 3.2.2, the effect of the baffle shape on the energy and cavitation performance of the RHCR is investigated by selecting the RHCR with 6 straight blades and a baffle position of 0.74. Figure 11 presents two computational domains of RHCRs with triangular baffles and circular baffles.

Figure 12 shows the influence of the baffle shape on the pressure distribution, bubble distribution and turbulence kinetic energy at the same time. The characteristics of the pressure field, bubble distribution and turbulence kinetic energy corresponding to the CCP with a triangular baffle have been elaborated in Sections 3.2.1 and 3.2.2.

(a) triangular baffle
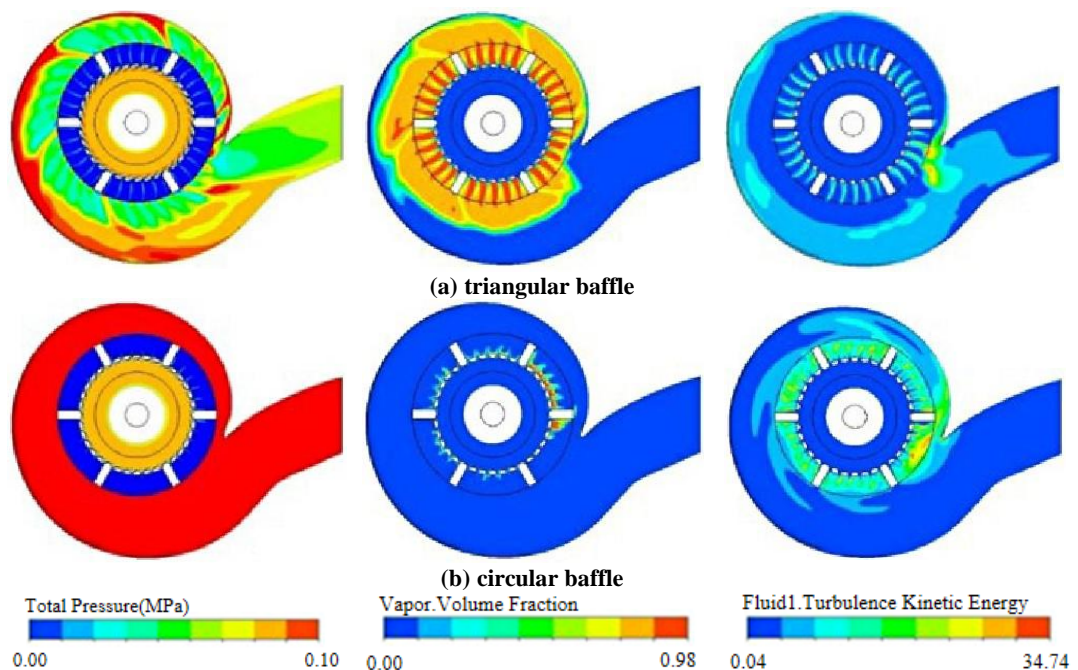

(b) circular baffle

Fig. 12. Effect of the baffle shape on the cavitating flow of CCP (left- pressure field; middle- cavitation distribution; right- turbulence kinetic energy).
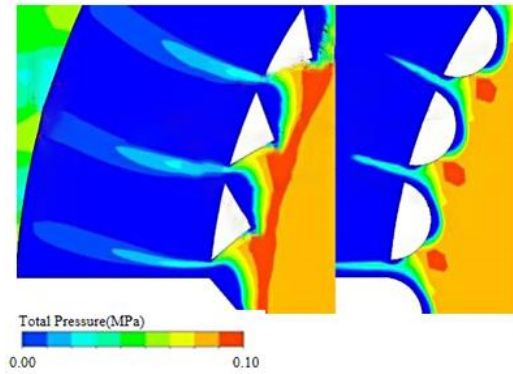
Fig. 13. Detailed pressure field at the throat of the triangular baffle and circular baffle (left- triangular baffle; right- circular baffle).

Fig. 14. Change of the head in the mass flow rate from 60 to 40 m³/h.

Compared with the triangular baffle, the pressure field of the RHCR with the circular baffle can be clearly divided into 3 zones, namely, upstream of the baffle, downstream of the baffle, and inside the volute. The pressure decreases after the liquid passes through the throat and recovers sharply and maintains a high pressure state throughout the volute, as shown in Fig. 12(b), left, which indicates that the liquid kinetic energy in the volute has been converted into pressure energy for good energy performance. It can be seen in Fig. 12(b), middle, that small amounts of bubbles are only induced on the side and downstream of the circular baffle, indicating that lower cavitation intensity is provided in this case, which can be reflected likewise in the turbulent kinetic energy, as shown in Fig. 12(b), right, where larger turbulence kinetic energy only exists downstream of the baffle due to the centralized collapse of bubbles. Figure 13 compares the detailed pressure field at the throat of the two baffles. The transition on the surface of the circular baffle is smoother than that on the surface of the triangular baffle, leading to a more prominent viscous effect between the liquid and the baffle, which makes the liquid flow adjacent to the wall, and the shedding is not obvious. In contrast, the liquid with circumferential velocity is more likely to fall off when it passes through the top due to the sharp shape of the triangular baffle, resulting in a larger low-pressure area on the side and downstream of the baffle, which is more likely to induce cavitation. Additionally, the circular baffle possesses less shrinkage and less throttling effect than the triangular baffle under the same throat size, so the cavitation area is significantly reduced.

In summary, the RHCR with a triangular baffle more easily induces cavitation and has a higher cavitation intensity than the RHCR with a circular baffle.

3.3 Energy Performance and Cavitation Development of the CCP

3.3.1 Energy Performance

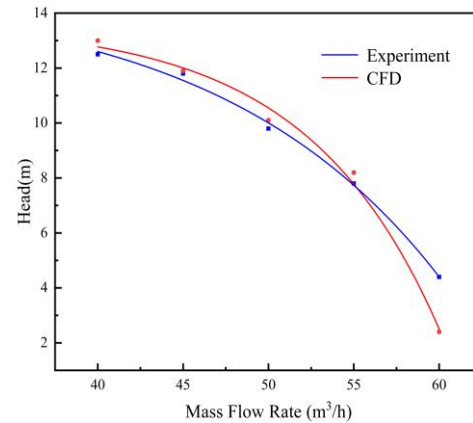Figure 14 demonstrates the effect of the mass flow rate on the head of the CCP. The head obviously increases by decreasing the mass flow rate from 60 m³/h to 40 m³/h, and the head exceeds 2 m in all cases, indicating good energy performance. The head predicted by the CFD method matches reasonably well with the experimental observation at most mass flow rates, and the head errors of the numerical calculation and experiment are mostly kept within 5%, showing that the calculation method is reliable again. The only large difference appears when the flow rate is 60 m³/h, indicating that the CFD method is an excessive prediction in the stage of severe cavitation, resulting in a lower head. In summary, the good consistency between the numerical and experimental results strongly confirms that the numerical method utilized in this study is highly believable.

3.3.2 Cavitation Development Process

To reveal the development of cavitation generated by this RHCR, some representative photos of one cycle are selected, as shown in Fig. 15, which clearly illustrates the cavitation development process in the RHCR, mainly including inception, growth, diffusion, shedding and ultimate collapse, in the photos, the yellow arrow indicates the moving direction of bubbles clusters. At $t_1=t_0+0.052T_{cycle}$ (T_{cycle} is the duration of cavitation development in a quasi-cycle, and the valve is 0.00444 s), multiscale bubbles first emerge at the outlet of the RHCR, as shown in Fig. 15(a). Then, the bubbles continue to grow, and the vapor volume fraction increases at $t_1=t_0+0.102T_{cycle}$, as shown in Fig. 15(b). After the bubbles are large enough to diffuse, the vapor volume fraction continuously increases at $t_1=t_0+0.424T_{cycle}$, which can be observed in Fig. 15(c). Experiencing two time intervals of diffusion, the bubble starts to shed due to the re-entrant flow, as shown in Fig. 15(d), and then collapses on account of high pressure in the volute, as shown in Fig. 15(e). After bubble collapse, small-scale bubbles at the outlet of the RHCR subsequently grow, followed by the next diffusion, and finally shed at $t_1=t_0+1T_{cycle}$, as shown in Fig. 15(f) to (h). Then, the next multiscale bubbles emerge simultaneously. The periodic generation and collapse of bubbles indicates that this RHCR has good cavitation performance.
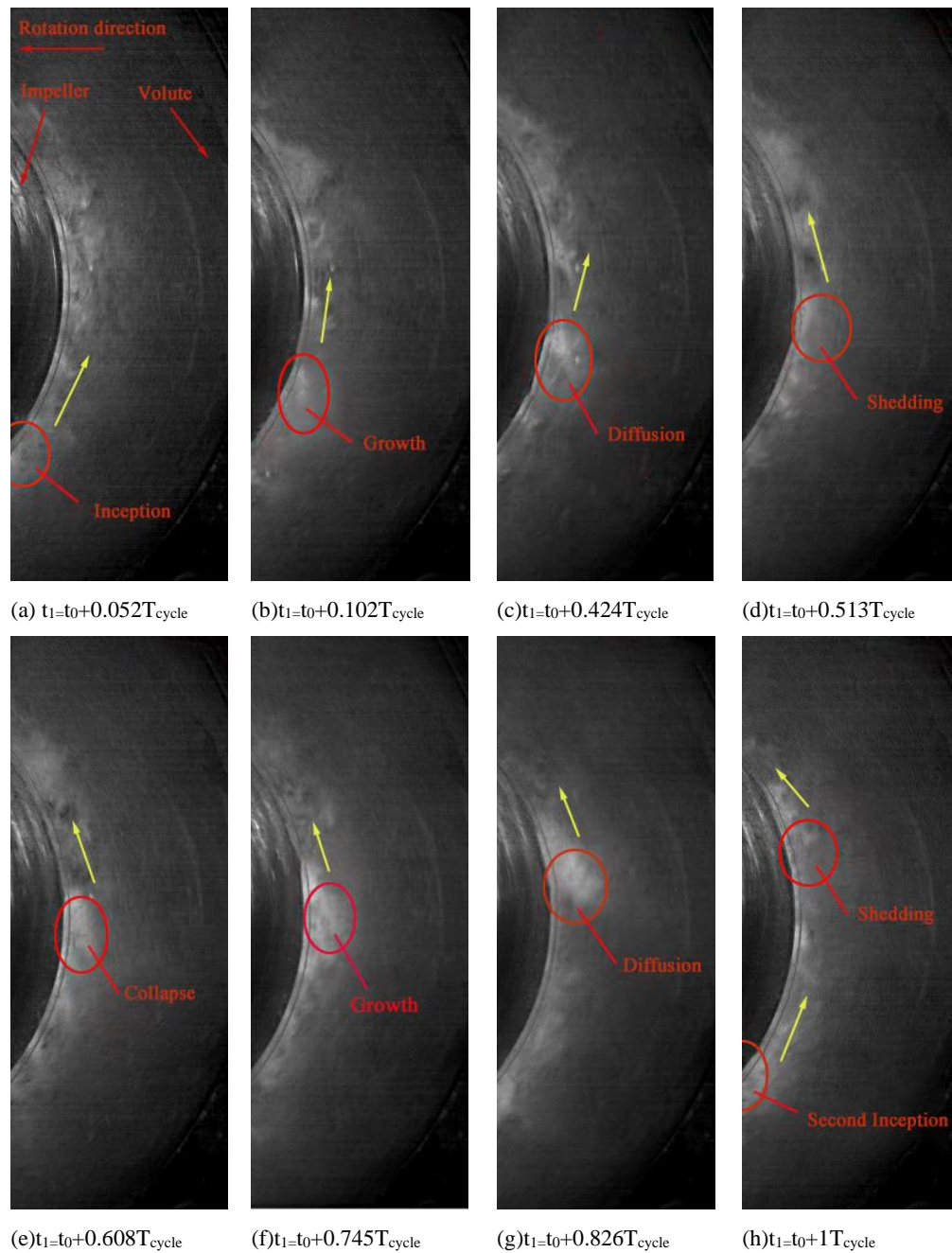
(a) $t_1 = t_0 + 0.052 T_{cycle}$ (b) $t_1 = t_0 + 0.102 T_{cycle}$ (c) $t_1 = t_0 + 0.424 T_{cycle}$ (d) $t_1 = t_0 + 0.513 T_{cycle}$

(e) $t_1 = t_0 + 0.608 T_{cycle}$ (f) $t_1 = t_0 + 0.745 T_{cycle}$ (g) $t_1 = t_0 + 0.826 T_{cycle}$ (h) $t_1 = t_0 + 1 T_{cycle}$

Fig. 15. Visualizations of cavitation development process.

4.   CONCLUSIONS

To obtain an excellent RHCR structure, this research investigates the effect of geometric structures, including the straight blade number, baffle position and baffle shape, on the cavitating flow of the RHCR by the CFD method and reveals the energy performance and cavitation development process of the optimized RHCR by experiment. The primary findings are as follows:

Increasing the straight blade number and the baffle position φ both increase the cavitation intensity; however, when the straight blade number exceeds 6 or the baffle position φ is greater than 0.74, a large number of bubbles with a high vapor volume fraction spread into the volute and even the volute outlet, which severely weaken the energy performance. The triangle baffle generates more intense cavitation than the circular baffle, and the RHCR with a straight blade number of 6, a baffle position of 0.74 and a triangular baffle shows better cavitation performance.

The head gradually increases with decreasing mass flow rate, and the numerical and experimental results of the head curve coincide well. The optimized RHCR shows good energy performance and cavitation performance, and the multiscale bubbles are induced by straight blades and baffles of the

optimized RHCR, accompanied by the twice quasi-periodic shedding dynamics in one cycle.

REFERENCES

Agarkoti, C., P. Thanekar and P. Gogate (2021). Cavitation based treatment of industrial wastewater: A critical review focusing on mechanisms, design aspects, operating conditions and application to real effluents. *Journal of Environmental Management* 300, 113786.

Badve, M. P., T. Alpar, A. B. Pandit, P. R. Gogate, L. Csoka (2015). Modeling the shear rate and pressure drop in a hydrodynamic cavitation reactor with experimental validation based on KI decomposition studies. *Ultrasonics Sonochemistry* 22, 272-277.

Badve, M., P. Gogate, A. Pandit and L. Csoka (2013). Hydrodynamic cavitation as a novel approach for wastewater treatment in wood finishing industry. *Separation and Purification Technology* 106, 15-21.

Bhukya, J., R. Naik, D. Mohapatra, L. K. Sinha and K. V. R. Rao (2021). Orifice based hydrodynamic cavitation of sugarcane juice: Changes in Physico-chemical parameters and Microbiological load. *LWT- Food Science and Technology* 150(1), 111909.

Charikleia, A., K. Bertaki, I. E. Triantaphyllidou, Z. Frontistis and D. V. Vayenas (2021). Treatment of real industrial-grade dye solutions and printing ink wastewater using a novel pilot-scale hydrodynamic cavitation reactor. *Journal of Environmental Management* 297, 113301.

Cheng, H. Y., X. P. Long, B. Ji, X. X. Peng and M. Farhat (2021). A new Euler-Lagrangian cavitation model for tip-vortex cavitation with the effect of non-condensable gas. *International Journal of Multiphase Flow* 134, 103441.

Dutta, N., P. Kopparthi, A. K. Mukherjee, N. Nirmalkar and G. Boczkaj (2021). Novel strategies to enhance hydrodynamic cavitation in a circular venturi using RANS numerical simulations. *Water research* 204, 117559.

Gagol, M., A. Przyjazny and G. Boczkaj (2018). Waste water treatment by means of advanced oxidation processes based on cavitation - A review. *Chemical Engineering Journal* 338, 599-627.

Gevari, M. T., M. Ghorbani, A. J. Svagan, D. Grishenkov and A. Kosar (2019). Energy harvesting with micro scale hydrodynamic cavitation-thermoelectric generation coupling. *Aip Advances* 9(10),11.

Ghorbani, M., A. Mohammadi, A. R. Motezakker, L. C. Villanueva, Y. Leblebici and A. Kosar (2017). Energy harvesting in microscale with cavitating flows. *Acs Omega* 2(10), 6870-6877.

Gostiša, J., B. Širok, S. K. Repinc, M. Levstek, M. Stražarc, B. Bizjan and M. Zupanc (2021a). Performance evaluation of a novel pilot-scale pinned disc rotating generator of hydrodynamic cavitation. *Ultrasonics Sonochemistry* 72(3), 105431.

Gostiša, J., M. Zupanc, M. Dular, B. Širok, M. Levstek and B. Bizjan (2021b). Investigation into cavitational intensity and COD reduction performance of the pinned disc reactor with various rotor-stator arrangements. *Ultrasonics Sonochemistry* 77, 105669.

Guan, X. F. (2011). *Modern Pump Theory and Design*. China Astronautic Publishing House, Beijing, China.

Kim, H., B. Koo, X. Sun and J. Y. Yong (2020). Investigation of sludge disintegration using rotor-stator type hydrodynamic cavitation reactor. *Separation and Purification Technology* 240, 116636.

Kosel, J., M. Šuštaršič, M. Petkovšek, M. Zupanc, M. Sežun and M. Dular (2020). Application of (super) cavitation for the recycling of process waters in paper producing industry. *Ultrasonics Sonochemistry* 64, 105002.

Li, M. C., G. Sankin and T. Vu (2021). Tri-modality cavitation mapping in shock wave lithotripsy. *Journal of the Acoustical Society of America* 149(2), 1258-1270.

Long, X. P., H. Y. Cheng, B. Ji, R. E. A. Arndt and X. X. Peng (2018). Large eddy simulation and Euler‐Lagrangian coupling investigation of the transient cavitating turbulent flow around a twisted hydrofoil. *International Journal of Multiphase Flow* 100, 41-56.

Long, Y., X. P. Long, B. Ji and T. Xing (2019). Verification and validation of Large Eddy Simulation of attached cavitating flow around a Clark-Y hydrofoil. *International Journal of Multiphase Flow* 115, 93-107.

Mevada, J., S. Devi and A. Pandit (2019). Large scale microbial cell disruption using hydrodynamic cavitation: energy saving options. *Biochemical Engineering Journal* 143, 151-160.

Patil, P. B., V. M. Bhandari and V. V. Ranade (2021). Improving efficiency for removal of ammoniacal nitrogen from wastewaters using hydrodynamic cavitation. *Ultrasonics Sonochemistry* 70, 105306.

Petkovšek, M., M. Mlakar, M. Levstek, M. Stražar, B. Širok and M. Dular (2015). A novel rotation generator of hydrodynamic cavitation for

waste-activated sludge disintegration. *Ultrasonics Sonochemistry* 26, 408-414.

Petkovšek, M., M. Zupanc, M. Dular, T. Kosjek, E. Heath, B. Kompare and B. Š irok (2013). Rotation generator of hydrodynamic cavitation for water treatment. *Separation and Purification Technology* 118, 415-423.

Ranade, V. V., V. P. Sarvothaman, A. Simpson and S. Nagarajan (2020). Scale-up of vortex based hydrodynamic cavitation devices: a case of degradation of di-chloro aniline in water. *Ultrasonics Sonochemistry* 70, 105295.

Reiner, M. (1949). On volume or isotropic flow as exemplified in the creep of concrete. *Applied Scientific Research Section a-Mechanics Heat Chemical Engineering Mathematical Methods* 1(5-6), 475-488.

Sawant, S. S., A. C. Anil, V. Krishnamurthy and C. Gaonkar (2008). Effect of hydrodynamic cavitation on zooplankton: A tool for disinfection. *Biochemical Engineering Journal* 42(3), 320-328.

Simpson, A. and V. V. Ranade (2018). Modelling of hydrodynamic cavitation with orifice: influence of different orifice designs. *Chemical Engineering Research & Design* 136, 698-711.

Smith, L. M. and W. C. Reynolds (1992). On the Yakhot–Orszag renormalization group method for deriving turbulence statistics and models. *Physics of Fluids A: Fluid Dynamics* 4(2), 364-390.

Song, Y., R. Hou, Z. Liu, J. Liu, W. Zhang and L. Zhang (2022). Cavitation characteristics analysis of a novel rotor-radial groove hydrodynamic cavitation reactor. *Ultrasonics Sonochemistry* 86, 106028.

Sun, X., J. J. Park, H. S. Kim, S. H. Lee, S. J. Seong, A. S. Om and J. Y. Yoon (2018). Experimental investigation of the thermal and disinfection performances of a novel hydrodynamic cavitation reactor. *Ultrasonics Sonochemistry* 49, 13–23.

Sun, X., J. Wang, H. Cheng, B. Ji and X. Long (2020a). Experimental study of the cavitation noise and vibration induced by the choked flow in a Venturi reactor. *Ultrasonics Sonochemistry* 67, 105183.

Sun, X., X. Jia, J. Liu and G. Wang (2020b). Investigation on the characteristics of an advanced rotational hydrodynamic cavitation reactor for water treatment. *Separation and Purification Technology* 251, 117252.

Sun, X., X. Xuan, Y. Song and X. Jia (2021a). Experimental and numerical studies on the cavitation in an advanced rotational hydrodynamic cavitation reactor for water treatment. *Ultrasonics Sonochemistry* 70, 105311.

Sun, X., W. You, X. Xuan and L. Ji (2021b). Effect of the cavitation generation unit structure on the performance of an advanced hydrodynamic cavitation reactor for process intensifications. *Chemical Engineering Journal* 412, 128600.

Sun, X., Z. Yang, X. Wei and Y. Tao (2021c). Multi-objective optimization of the cavitation generation unit structure of an advanced rotational hydrodynamic cavitation reactor. *Ultrasonics Sonochemistry* 80, 105771.

Taba, B., J. B. Jam, C. Cabb, E. V. Canettieri and C. E. Tuna (2020). Theoretical modeling and experimental validation of hydrodynamic cavitation reactor with a Venturi tube for sugarcane bagasse pretreatment. *Bioresource Technology* 311, 123540.

Wang, Z. Y., H. Y. Cheng and B. Ji (2021a) Euler‑Lagrange study of cavitating turbulent flow around a hydrofoil. *Physics of Fluids* 33(11), 112108.

Wang, B., H. Su and B. Zhang (2021b). Hydrodynamic cavitation as a promising route for wastewater treatment– A review. *Chemical Engineering Journal* 412(3-4), 128685.

Wang, Z. Y., H. Y. Cheng and B. Ji (2022) Numerical prediction of cavitation erosion risk in an axisymmetric nozzle using a multi-scale approach. *Physics of Fluids* 34(6), 062112.

Zupanc, M., T. Kosjek, M. Petkovšek, M. Dular, B. Kompare, B. Širok, M. Stražar and E. Heath (2014). Shear-induced hydrodynamic cavitation as a tool for pharmaceutical micropollutants removal from urban wastewater. *Ultrasonics Sonochemistry* 21(3), 1213-1221.

Zwart, P. J., A. G. Gerber and T. Belamri (2004, January). A two-phase flow model for predicting cavitation dynamics. In *Fifth International Conference on Multiphase Flow*, Yokohama, Japan.